

Single-Particle Model for a Lithium-Ion Cell: Thermal Behavior

Meng Guo, Godfrey Sikha and Ralph E. White

J. Electrochem. Soc. 2011, Volume 158, Issue 2, Pages A122-A132.
doi: 10.1149/1.3521314

**Email alerting
service**

Receive free email alerts when new articles cite this article - sign up in the box at the top right corner of the article or [click here](#)

To subscribe to *Journal of The Electrochemical Society* go to:
<http://jes.ecsdl.org/subscriptions>

© 2010 ECS - The Electrochemical Society



Single-Particle Model for a Lithium-Ion Cell: Thermal Behavior

Meng Guo,^a Godfrey Sikha,^{b,*} and Ralph E. White^{a,**,z}

^aDepartment of Chemical Engineering, University of South Carolina, Columbia, South Carolina 29208, USA

^bApplied Materials, Incorporated, Santa Clara, California 95054, USA

The single-particle model presented by Santhanagopalan et al. [*J. Power Sources*, **156**, 620 (2006)] is extended to include an energy balance. The temperature dependence of the solid phase diffusion coefficient of the lithium in the intercalation particles, the electrochemical reaction rate constants, and the open circuit potentials (OCPs) of the positive and negative electrodes are included in the model. The solution phase polarization is approximated using a nonlinear resistance, which is a function of current and temperature. The model is used to predict the temperature and voltage profiles in a lithium-ion cell during galvanostatic operations. The single-particle thermal model is validated by comparing the simulated voltage and temperature profiles to the results obtained using a distributed porous electrode model. The simulation results from the single-particle thermal model also show good agreement with experimental voltage data obtained from lithium-ion pouch cells under different discharge rates (C/33, C/2 and C) at different temperatures (15, 25, 35, and 45°C).

© 2010 The Electrochemical Society. [DOI: 10.1149/1.3521314] All rights reserved.

Manuscript submitted January 25, 2010; revised manuscript received July 22, 2010. Published December 15, 2010; publisher error corrected February 3, 2011.

Several thermal models for lithium-ion cells have been presented in the literature; for example, Newman and Pals^{1,2} presented cell and battery stack thermal models incorporating the pseudo two-dimensional porous electrode model^{3,4} (P2D model) with an energy balance,^{5,6} in which the isothermal and adiabatic discharge behaviors were studied. In 1999, Botte et al.⁴ developed a pseudo two-dimensional (2D) thermal model for $\text{Li}_x\text{C}_6/\text{LiNiO}_2$ cells, in which the temperature dependence of parameters⁷⁻¹⁰ were considered and the effects of parameters on the predicted cell temperature were included. In 2003, Srinivasan and Wang¹¹ developed a 2D thermal model for large lithium-ion cells, in which the energy balance equation and the porous electrode model with polynomial approximations (PP model) for the solid phases were integrated. In this model, experimentally measured entropy data¹²⁻¹⁴ for electrochemical reactions were also incorporated. In 2008, Kumaresan et al.¹⁵ developed a thermal model for the LiCoO_2 -mesocarbon microbead (MCMB) pouch cells based on the PP model and obtained good agreement between model predictions and experimental data.

A disadvantage common to the P2D model and the PP model is the long simulation time due to the large number of nonlinear equations, so these models become computationally inefficient for simulating conditions such as cycling behavior and series/parallel configuration of stacked cells in battery packs. To improve computational run time without compromising accuracy, the single-particle model (SP model) (Ref. 3 and 16) was proposed. The SP model ignores the detailed distribution of local concentration and potential in the solution phase and instead accounts for a lumped solution resistance term. Furthermore, the local reaction currents across the porous electrode are assumed to be constant, which allows treatment of a porous electrode as a large number of single particles, all of which are subjected to the same conditions. These assumptions are reasonable for low applied current densities, thin electrodes, and highly conductive electrodes. In such cases the overpotential is primarily affected by the diffusion in the solid state. At high current densities, the concentration gradients in the electrolyte become important. The model presented here does not include these concentration gradients and is consequently limited to low to moderate current densities. These assumptions simplify the model equations significantly. The SP model (using a two term polynomial approximation) shows good agreement with the detailed PP model for charge/discharge below 1C, where C denotes the cell capacity.³ In

this work, the single-particle model is extended to include thermal effects by adding the energy balance equation to the SP model. Instead of using a two term polynomial approximation, the solid phase diffusion equations are solved by the eigenfunction expansion method, which improved the accuracy of the model. Parameters in this SP thermal model are estimated by fitting the simulated discharge curves (up to 1C rate) with the experimental data obtained on lithium-ion pouch cells. Also, good agreement between the SP thermal model and the PP thermal model (presented in Ref. 15) is obtained.

Mathematical Model

The solid phase diffusion.— In the SP model, electrodes are assumed to consist of spherical intercalation particles with identical size. The key assumption in the single-particle model is that the current distribution is taken to be uniform along the thickness of the porous electrode. Newman and Tobias¹⁷ derived expressions to calculate the reaction current distribution along the thickness of porous electrode. To validate the assumption of uniform current density distribution, the reaction current distribution was evaluated for the case of ohmically limited system [using Eq. 18 in Ref. 17] using the parameter values for this system. The calculations showed that the reaction current distribution due to the electrochemical reaction was fairly uniform. Therefore, each entire porous electrode (positive/negative) can be represented by a single intercalation particle. The mass balance of lithium ions in an intercalation particle of electrode active material is described by Fick's second law in a spherical coordinate system¹⁶

$$\frac{\partial c_{s,j}}{\partial t} = \frac{D_{s,j}}{r^2} \frac{\partial}{\partial r} \left(r^2 \frac{\partial c_{s,j}}{\partial r} \right) \quad [1]$$

where $c_{s,j}$ is the concentration of lithium ions in the intercalation particle, t is time, r is the radius direction coordinate, $D_{s,j}$ is the solid phase diffusion coefficient, which is a function of temperature, and the subscript $j = p/n$ represents the positive/negative electrode.

The maximum concentration is determined by ρ and m . The maximum concentration for lithium in the particles is calculated based on the density, molecular mass, and the maximum lithium stoichiometry of the electrode

$$c_{s,j}(t=0) = c_{s,ini,j} \quad [2]$$

The mass flux of lithium ions at the center of the spherical particle ($r = 0$) is zero due to the symmetry, so

* Electrochemical Society Active Member.

** Electrochemical Society Fellow.

^z E-mail: white@cec.sc.edu

$$\left(D_{s,j} \frac{\partial c_{s,j}}{\partial r}\right)_{r=0} = 0 \quad [3]$$

and the other boundary condition at particle surface ($r = R_j$) is

$$\left(D_{s,j} \frac{\partial c_{s,j}}{\partial r}\right)_{r=R_j} = -J_j \quad [4]$$

where J_j is the molar flux of lithium ions at the surface and can be expressed as

$$J_p = \frac{I}{FS_p} \quad J_n = -\frac{I}{FS_n} \quad [5]$$

where I is the total current passing through the cell tabs and is defined in this work as positive for charge process and negative for discharge process and S_j is the total electroactive surface area of electrode j

$$S_j = \frac{3\varepsilon_j V_j}{R_j} \quad [6]$$

where ε_j is the volume fraction of solid phase active material in electrode j and V_j is the total volume of that electrode.

The state of charge (SoC) for positive and negative electrodes is defined as the local lithium-ion concentration divided by the maximum intercalable lithium-ion concentration

$$x_j = \frac{c_{s,j}}{c_{s,j,\max}} \quad (j = p, n) \quad [7]$$

The initial and surface SoCs for positive and negative electrodes are defined, respectively, as

$$x_{\text{ini},j} = \frac{c_{s,\text{ini},j}}{c_{s,j,\max}} \quad (j = p, n) \quad [8]$$

$$x_{j,\text{surf}} = \frac{c_{s,j}|_{r=R_j}}{c_{s,j,\max}} \quad (j = p, n) \quad [9]$$

As shown in Eq. 8 and 9, the initial SoC $x_{\text{ini},j}$ is a constant while the surface SoC $x_{j,\text{surf}}$ is only a function of time.

Electrochemical reaction kinetics.—The electrochemical reactions for lithium-ion intercalation/deintercalation at the solid/solution interface can be expressed as



where θ_s represents a vacant host on the solid particle surface. The rate of such a reaction is related to the surface SoC $x_{j,\text{surf}}$ and the overpotential η_j and is expressed through the Butler–Volmer equation (Appendix A)

$$J_j = k_j c_{s,j,\max} c_e^{0.5} (1 - x_{j,\text{surf}})^{0.5} x_{j,\text{surf}}^{0.5} \left[\exp\left(\frac{0.5F}{RT} \eta_j\right) - \exp\left(-\frac{0.5F}{RT} \eta_j\right) \right] \quad (j = p, n) \quad [11]$$

where k_j is the temperature-dependent reaction rate constant and the electrolyte concentration in solution phase c_e is assumed to be a constant in the SP model. The overpotential η_j is defined as

$$\eta_j = \phi_{1,j} - \phi_{2,j} - U_j$$

$$(j = p, n) \quad [12]$$

where $\phi_{1,j}$ is the solid phase potential, $\phi_{2,j}$ is the solution phase potential, and U_j is the OCP depending on both the surface SoC and temperature. In this work, the solution phase was simplified as a nonlinear resistor, so the potential drop in the solution phase between the positive and negative electrodes can be expressed as

$$\phi_{2,p} - \phi_{2,n} = IR_{\text{cell}} \quad [13]$$

The electrolyte resistance, R_{cell} , is actually determined by a complex mass and charge transfer processes in the solution phase;¹⁸ the value of this parameter is assumed to depend on cell temperature and current; the approximation of R_{cell} is discussed later. The cell voltage equals to the difference of solid phase potential between the positive and negative electrodes

$$V_{\text{cell}} = \phi_{1,p} - \phi_{1,n} \quad [14]$$

By using the inverse hyperbolic function on Eq. 11, a more explicit expression of cell voltage is

$$V_{\text{cell}} = U_p(x_{p,\text{surf}}, T) - U_n(x_{n,\text{surf}}, T) + \frac{2RT}{F} \ln\left(\frac{\sqrt{m_p^2 + 4} + m_p}{2}\right) + \frac{2RT}{F} \ln\left(\frac{\sqrt{m_n^2 + 4} + m_n}{2}\right) + IR_{\text{cell}} \quad [15]$$

where

$$m_p = \frac{I}{Fk_p S_p c_{s,p,\max} c_e^{0.5} (1 - x_{p,\text{surf}})^{0.5} x_{p,\text{surf}}^{0.5}}$$

$$m_n = \frac{I}{Fk_n S_n c_{s,n,\max} c_e^{0.5} (1 - x_{n,\text{surf}})^{0.5} x_{n,\text{surf}}^{0.5}}$$

The format of Eq. 15 enables us to directly obtain the analytical Jacobian matrix of V_{cell} with respect to parameters, and the computation efficiency in the parameter estimation is greatly improved.

The energy balance.—In this model, the spatial temperature distribution in cell is neglected, so the cell temperature T is a function of time only. The general energy balance equation is given as Eq. 24 in Ref. 2, and in this work, it is written as

$$\rho v C_p \frac{dT}{dt} = IT \left[\frac{\partial U_p}{\partial T}(x_{p,\text{surf}}) - \frac{\partial U_n}{\partial T}(x_{n,\text{surf}}) \right] + I(\eta_p - \eta_n + IR_{\text{cell}}) - q \quad [16]$$

The initial cell temperature is assumed to be same with the ambient temperature

$$T|_{t=0} = T_{\text{amb}} \quad [17]$$

where T is the cell temperature, v is the volume of cell, ρ is the density of cell, C_p is the specific heat capacity of cell, and q is the rate of heat transfer between cell and surroundings. In this work, heat flux at cell surface are assumed to follow Newton's law of cooling, so the term q is expressed as

$$q = hA(T - T_{\text{amb}}) \quad [18]$$

where h is the heat transfer coefficient and A is the cell surface area. On the right hand side of Eq. 16, the first term $IT[\partial U_p/\partial T(x_{p,\text{surf}}) - \partial U_n/\partial T(x_{n,\text{surf}})]$ is the reversible heat caused by the reaction entropy change. The value of the reversible heat can be either positive or negative depending on the direction of electrode reactions. The second term on the right hand side of Eq. 16, $I(\eta_p - \eta_n + IR_{\text{cell}})$, is the irreversible heat generated from electrode polarization. The irreversible heat generated is always positive for both forward and reverse reactions. The third term q on the right hand side of Eq. 16 represents the heat exchanged between the cell and the surroundings. The variation of cell temperature depends on the combined contribution of reversible and irreversible heats as well as the heat exchange between the cell and the surroundings.

Temperature dependency of parameters.— The transport and kinetic parameters involved in the model equations are functions of temperature; and such dependences of these parameters on cell temperature were included in this thermal model. Generally, the solid phase diffusion coefficients $D_{s,j}$ and the reaction rate constants k_j depend on the temperature through Arrhenius' correlation^{4,7-10}

$$D_{s,j}(t) = D_{s,j,\text{ref}} \exp \left[\frac{E_{a,d,j}}{R} \left(\frac{1}{T} - \frac{1}{T_{\text{ref}}} \right) \right] \quad [19]$$

$$k_j(t) = k_{j,\text{ref}} \exp \left[\frac{E_{a,r,j}}{R} \left(\frac{1}{T} - \frac{1}{T_{\text{ref}}} \right) \right] \quad [20]$$

(j = p, n)

where T_{ref} is the reference temperature, $D_{s,j,\text{ref}}$ is the solid phase diffusion coefficient of electrode j at the reference temperature, $k_{j,\text{ref}}$ is the reaction rate constant of electrode j at the reference temperature, $E_{a,d,j}$ is the diffusion coefficient activation energy of electrode j , $E_{a,r,j}$ is the reaction rate activation energy of electrode j , and R is the ideal gas constant. As mentioned above, the cell temperature varies only with time, so $D_{s,j}$ and $k_{j,\text{ref}}$ are all functions of time only. The OCP U_p and U_n are the functions of both the SoC and temperature, and the correlation can be approximated by Taylor's expansion

$$U_j(x_{j,\text{surf}}, T) = U_j(x_{j,\text{surf}}, T_{\text{ref}}) + \left. \frac{\partial U_j}{\partial T} \right|_{x_{j,\text{surf}}, T_{\text{ref}}} (T - T_{\text{ref}}) \quad [21]$$

(j = p, n)

Solution procedure.— *Analytical techniques to solve for concentration in the single-particle model.*— As shown above, this thermal model includes two partial differential equations describing the solid phase diffusion for each electrode and an ordinary differential equation (ODE) for the overall cell energy balance. These equations are coupled together by the nonlinear dependence of transport and kinetic parameters on cell temperature; so, no analytical solution can possibly be obtained for this equation system when the variation of the cell temperature is taken into account. However, Eq. 1 can be solved using the eigenfunction expansion method (see Appendix B) to obtain a solution with the following form

$$x_j = x_{\text{ini},j} + \frac{\bar{r}_j^2}{2} \delta_j(t) - \frac{3}{10} \delta_j(t) + 3 \int_0^t \left[\frac{D_{s,j}(\tau)}{R_j^2} \delta_j(\tau) \right] d\tau + \sum_{k=1}^{\infty} \frac{\sin(\lambda_k \bar{r}_j)}{\bar{r}_j \sin \lambda_k} \left[u_{j,k}(t) - \frac{2\delta_j(t)}{\lambda_k^2} \right] \quad [22]$$

where $\bar{r}_j = r/R_j$ is the dimensionless radius coordinate, τ is the dummy variable of integration, and $\delta_j(t)$ is the dimensionless lithium flux. The SoC at the surface of intercalation particle is

$$x_{j,\text{surf}} = x_j|_{\bar{r}_j=1} = x_{\text{ini},j} + \frac{1}{5} \delta_j(t) + 3 \int_0^t \left[\frac{D_{s,j}(\tau)}{R_j^2} \delta_j(\tau) \right] dt + \sum_{k=1}^{\infty} \left[u_{j,k}(t) - \frac{2\delta_j(t)}{\lambda_k^2} \right] \quad [23]$$

where the eigenvalues λ_k are roots of the following algebraic equation

$$\sin \lambda_k - \lambda_k \cos \lambda_k = 0 \quad [24]$$

Due to the periodicity, the value of λ_k becomes infinitely large as the subscript number k increases. The eigenfunctions $u_{j,k}$ are determined by the following ordinary differential equations

$$\frac{du_{j,k}(t)}{dt} = - \frac{\lambda_k^2 D_{s,j}(t)}{R_j^2} u_{j,k} + 2 \frac{D_{s,j}(t)}{R_j^2} \delta_j(t)$$

$$u_{k,j}(0) = 0$$

$$k = 1, \dots, \infty$$

$$j = p, n \quad [25]$$

As a result, the model is reduced to a system of ODEs shown in Eq. 16 and 25, from which the dependant variables T and $u_{k,j}$ are solved, while other variables involved in the model, such as the SoC, OCP, and cell voltage can all be expressed as the functions of T and $u_{k,j}$. In the case when current I and cell temperature T are both constants, there exist analytical solutions for Eq. 25

$$u_{k,j} = 2 \frac{D_{s,j}}{R_j^2} \delta_j \left[1 - \exp \left(- \frac{\lambda_k^2 D_{s,j}}{R_j^2} t \right) \right] \quad [26]$$

Substituting Eq. 26 into Eq. 22 yields the analytical solution for solid phase diffusion

$$x_j = x_{\text{ini},j} + \delta_j \left[3 \frac{D_{s,j}}{R_j^2} t + \frac{1}{10} (5\bar{r}_j^2 - 3) - \frac{2}{\bar{r}_j} \sum_{k=1}^{\infty} \frac{\sin(\lambda_k \bar{r}_j)}{\lambda_k^2 \sin(\lambda_k)} \times \exp \left(- \frac{\lambda_k^2 D_{s,j}}{R_j^2} t \right) \right] \quad [27]$$

and the SoC at particle surface is expressed as follows

$$x_{j,\text{surf}} = x_{\text{ini},j} + \delta_j \left[3 \frac{D_{s,j}}{R_j^2} t + \frac{1}{5} - \frac{2}{\lambda_k^2} \sum_{k=1}^{\infty} \exp \left(- \frac{\lambda_k^2 D_{s,j}}{R_j^2} t \right) \right] \quad [28]$$

(j = p, n)

Eq. 27 and 28 are consistent with the analytical solutions derived by Subramanian and White using the separation of variables method.¹⁹

The solution accuracy.— The mathematical model described by Eq. 1-28 was solved using the backward differentiation formula method with MATLAB. The first issue regarding this model is the accuracy and efficiency in simulations. According to Eq. 24, the solution for solid phase diffusion theoretically includes an infinite series of eigenfunctions $u_{k,j}$, but this infinite series must be truncated in running a practical model to save simulation time and computer memory. Obviously, keeping a large number of terms in the series will ensure high accuracy for the solution; however, the more the eigenfunctions are kept, the longer it will take to converge; so, there has to be a compromise between the accuracy and efficiency. In this work, the solution for an equation system including 2000 eigenfunctions is regarded as the complete solution for the model, and the truncated solutions with 1, 5, 10, and 20 eigenfunctions are compared with the complete solution. The summary of equations and input variable values are presented in Table 1. The profiles of first five eigenfunctions for both positive and negative electrodes in a 1C discharge starting with 25°C are presented in Fig. 1. As shown in the plots, there are no steady states for the eigenfunctions because the solid phase diffusion coefficients keep changing with the cell temperature. In such a case, it often requires more terms in the series for an unstable model than for a stable one to ensure the accuracy. The V_{cell} versus time curves from solutions with different numbers of eigenfunctions (ambient temperature is 25°C) are presented in Fig. 2a, and the plots of the relative error between the truncated solutions and the complete solution are presented in Fig. 2b, where the relative error is defined as

$$\text{Relative error} = \frac{|V_{\text{cell},k} - V_{\text{cell,complete}}|}{V_{\text{cell,complete}}} \quad [29]$$

where $V_{\text{cell},k}$ is the cell voltage calculated from k eigenfunctions and $V_{\text{cell,complete}}$ is the cell voltage calculated from the complete solution. We can find from Fig. 1 that when the number of eigenfunctions is more than (or equal to) 10, the relative error will be less than 10^{-5} except for the first point; therefore, the number of eigenfunctions

Table I. Equations and input variables for the model.

ODEs	$\frac{du_{k,p}(t)}{dt} = -\frac{\lambda_k^2 D_{s,p}(t)}{R_p^2} u_{k,p}(t) + 2 \frac{D_{s,p}(t)}{R_p^2} \delta_p(t)$ $u_{k,p}(0) = 0$
	$\frac{du_{k,n}(t)}{dt} = -\frac{\lambda_k^2 D_{s,n}(t)}{R_n^2} u_{k,n}(t) + 2 \frac{D_{s,n}(t)}{R_n^2} \delta_n(t)$ $u_{k,n}(0) = 0$
	$k = 0, \dots, N$
	$\rho v C_p \frac{dT}{dt} = IT \left[\frac{\partial U_p}{\partial T}(x_{p,surf}) - \frac{\partial U_n}{\partial T}(x_{n,surf}) \right] + I \{ V_{cell} - [U_p(x_{p,surf}, T) - U_n(x_{n,surf}, T)] \} - hA(T - T_{amb})$ $T(0) = T_{amb}$
Expressions	$x_{j,surf} = x_{ini,j} + \frac{1}{5} \delta_j(t) + 3 \int_0^t \left[\frac{D_{s,j}(\tau)}{R_j^2} \delta_j(\tau) \right] d\tau$ $+ \sum_{k=1}^N \left[u_{j,k}(t) - \frac{2\delta_j(t)}{\lambda_k^2} \right]$
	$\delta_p(t) = -\frac{IR_p}{S_p F D_{s,p}(t) c_{s,p,max}} \quad \delta_n(t) = \frac{IR_n}{S_n F D_{s,n}(t) c_{s,n,max}}$
	$V_{cell} = U_p(x_{p,surf}, T) - U_n(x_{n,surf}, T) + \frac{2RT}{F}$
	$\times \ln \left(\frac{\sqrt{m_p^2 + 4} + m_p}{2} \right) + \frac{2RT}{F} \ln \left(\frac{\sqrt{m_n^2 + 4} + m_n}{2} \right) + IR_{cell}$
	$m_p = \frac{I}{F k_p S_p c_{s,p,max} c_e^{0.5} (1 - x_{p,surf})^{0.5} x_{p,surf}^{0.5}}$
	$m_n = \frac{I}{F k_n S_n c_{s,n,max} c_e^{0.5} (1 - x_{n,surf})^{0.5} x_{n,surf}^{0.5}}$
	$D_{s,j}(t) = D_{s,j,ref} \exp \left[\frac{E_{a,d,j}}{R} \left(\frac{1}{T} - \frac{1}{T_{ref}} \right) \right]$
	$k_j(t) = k_{j,ref} \exp \left[\frac{E_{a,r,j}}{R} \left(\frac{1}{T} - \frac{1}{T_{ref}} \right) \right]$
	$U_j(x_{j,surf}, T) = U_j(x_{j,surf}, T_{ref}) + \left. \frac{\partial U_j}{\partial T} \right _{x_{j,surf}, T_{ref}} (T - T_{ref})$
	$R_{cell} = \theta_1 + \theta_2 (T - T_{amb})$ $(j = p, n)$
Input variables	$N = 1, 5, 10, 20, 2000$
	$I = -1.656 \text{ A (1C)}$
	$T_{amb} = 298 \text{ K}$
	$x_{ini,p} = 0.4952$
	$x_{ini,n} = 0.7522$
	$\theta_1 = 0.0162 \text{ } \Omega$
	$\theta_2 = 0.0162 \text{ } \Omega/\text{K}$

will be kept as 10 for all the simulations with this model in the following procedures.

Parameter estimation.— To check the agreement of the theoretical model with the experimental data obtained on the lithium-ion pouch cell, the values of certain parameters in this model need to be estimated. The first step of this procedure is to fit the C/33 discharge curves at four ambient temperatures (15, 25, 35, and 45°C); at the very low discharge rate, the cell temperature can be regarded as the same with the constant ambient temperature all the time, so the analytical solution presented in Eq. 27 can be used directly; furthermore, with constant temperature and current, the solution phase resistance can also be regarded as a constant. Therefore, by fitting the C/33 discharge curves, three parameters will be estimated simultaneously: the initial SoCs for the positive and negative electrodes ($x_{ini,p}$ and $x_{ini,n}$) and the solution phase resistance (R_{cell}).

After the parameter estimation on low rates, the single-particle thermal model was then used to fit the discharge curves for higher rates. The initial SoC of the individual electrodes obtained from C/33 rate discharge data can also be used as initial conditions in the

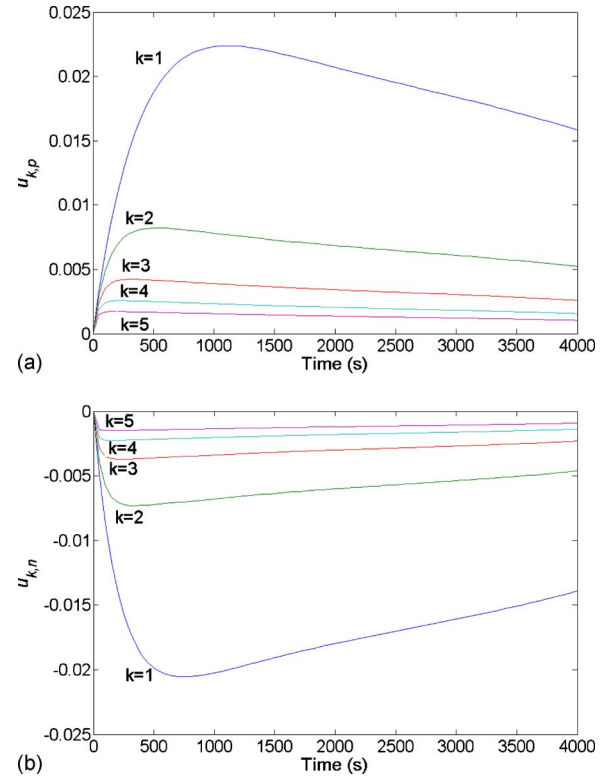


Figure 1. (Color online) Plot for eigenfunctions during 1C discharge at 25°C. (a) Positive electrode eigenfunctions and (b) negative electrode eigenfunctions.

model for the C/2 and C/1 rates. The solution phase resistance, R_{cell} , will vary with both current and cell temperature, and first order Taylor's expansion was used to approximate such variations

$$R_{cell}(I, T) = R(I = 0, T = T_{amb}) + \left. \frac{\partial R_{cell}}{\partial I} \right|_{I=0, T=T_{amb}} I + \left. \frac{\partial R_{cell}}{\partial T} \right|_{I=0, T=T_{amb}} (T - T_{amb}) + \left. \frac{\partial^2 R_{cell}}{\partial I \partial T} \right|_{I=0, T=T_{amb}} I(T - T_{amb}) \quad [30]$$

When the current is constant, Eq. 30 can be rearranged as

$$R_{cell}(I, T) = \theta_1 + \theta_2 (T - T_{amb}) \quad [31]$$

where parameter θ_1 and θ_2 are expressed as follows

$$\theta_1 = R(I = 0, T = T_{amb}) + \left. \frac{\partial R_{cell}}{\partial I} \right|_{I=0, T=T_{amb}} I \quad [32]$$

$$\theta_2 = \left. \frac{\partial R_{cell}}{\partial T} \right|_{I=0, T=T_{amb}} + \left. \frac{\partial^2 R_{cell}}{\partial I \partial T} \right|_{I=0, T=T_{amb}} I \quad [33]$$

In fitting each of the C/2 and C/1 discharge curves (at 15, 25, 35, and 45°C), θ_1 and θ_2 were estimated as parameters using the Gauss Newton method. In fitting 1C discharge curves, the heat transfer coefficient h was adjusted to obtain agreement of the predicted cell temperature profiles with those from the PP model.¹⁵

Experimental

All the experimental data used in this work were collected from Mine Safety Appliances (nameplate capacity $C = 1.656 \text{ Ah}$) pouch cells and the testings were done in-house. Prior to cycling, batches of cells were equilibrated in the environmental chambers at the pre-determined temperatures (15, 25, 35, and 45°C). To obtain the initial

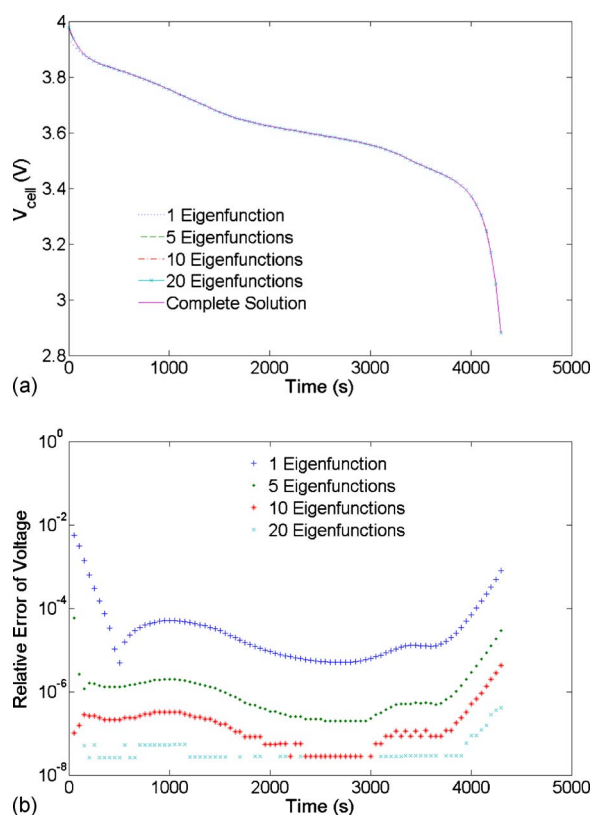


Figure 2. (Color online) (a) The discharge curves from solutions with different number of eigenfunctions (1C discharge at 25 °C). (b). The relative error between truncated solutions and complete solution.

cell capacities at various temperatures and charge/discharge rates, the following protocols were used. The discharge protocol consists of galvanostatic discharge current corresponding to the three discharge rates (C/33, C/2 and C/1) until the cutoff voltage of 3.3 V was reached. The capacity values at the cutoff voltage were taken as the fresh cell discharge capacity at the different rates. The charge protocols are slightly different for the different rates. For C/33 rate measurement, the cells were charged to 4.1 V, followed by a rest for 30 min before being discharged back to 3.3 V. For C/2 and C/1 rates, the cells were charged at respective currents to 4.1 V and then potentiostatically held at the cutoff voltage until the current tapered down to 50 mA. For C/2 and C/1 discharges, the cells were discharged at respective constant current rate to 3.3 V, then kept open circuit for 30 minutes, and then discharged at C/33 rate until the voltage reached 3.3 V to make sure that the subsequent charge starts at the same state of charge. The values of design parameters for this type of pouch cells are listed in Table II, and detailed experimental procedures involved in cycling protocols and periodic performance tests are available in Ref. 15. According to the authors of Ref. 15, because the cells were charged at the respective ambient temperatures, the extent of charging could be different, which subsequently causes the initial states of discharge to be different for cells at different temperatures.

Results and Discussion

Comparison between simulation and experimental data for discharge profiles.— In fitting the C/33 rate discharge curves, the computation was performed by the LSQNONLIN subroutine in MATLAB. The simulated versus experimental C/33 discharge curves with estimated parameter values ($x_{ini,p}$, $x_{ini,n}$, and constant R_{cell}) are presented in Figs. 3a–3d. As stated in Ref. 15, the cells were charged at their respective ambient temperatures (i.e., at 15, 25, 35, and 45 °C). Therefore, the initial states of charge vary. In each figure, the solid

Table II. The cell parameter values used in this model.

Symbol	$j = p$	$j = n$	Unit
L_j	70	73.5	μm
S_j	1.1167 ^a	0.7824 ^a	m^2
$c_{s,j,\text{max}}$	51,410 ^a	31,833 ^a	mol/m^3
R_j	8.5×10^{-6a}	12.5×10^{-6a}	m
$k_{j,\text{ref}}$	6.6667×10^{-11b}	1.764×10^{-11b}	$\text{m}^{2.5} \text{mol}^{-0.5} \text{s}^{-1}$
$E_{a,\text{re},j}$	58 ^c	20 ^d	kJ/mol
$D_{s,j,\text{ref}}$	1.0×10^{-14c}	3.9×10^{-14c}	m^2/s
$E_{a,\text{di},j}$	29 ^f	35 ^g	kJ/mol
$\alpha_{a,j}$	0.5	0.5	
$\alpha_{c,j}$	0.5	0.5	
c_e		1000 ^a	mol/m^3
F		96,487	C/mol
ρ		1626 ^a	kg/m^3
v		$0.199 \times 0.08499 \times 0.002^a$	m^3
C_p		750 ^h	$\text{J}/(\text{K}\cdot\text{kg})$
T_{ref}		25	$^{\circ}\text{C}$
R		8.3143	$\text{J}/(\text{mol}\cdot\text{K})$
hA		0.085	$\text{J}/(\text{s}\cdot\text{K})$
L_s		25	μm

^a Calculated or obtained directly from cell design parameters.

^b Ref. 15.

^c Ref. 10.

^d Ref. 8.

^e Ref. 3.

^f Ref. 7.

^g Ref. 9.

^h Assumed values

curve is the prediction of the analytical solution described by Eq. 28, the dashed-and-dotted curve is the prediction of the PP model.¹⁵ the dashed curve is the simulated open circuit voltage for each cell, and the dotted curve is the experimental data. The discharge capacity of cell is defined as

$$\text{Cap} = \frac{1}{3600} \int_0^{t_{\text{final}}} |I| dt \quad [34]$$

where t_{final} is the time at the end of the discharge. Since the electrode polarization is almost negligible at the very low current densities, the voltage profiles of cells at C/33 rate are very similar to the open circuit voltage curves. It is also interesting to note, in Figs. 3a–3d, that the single-particle thermal model fits the experimental data better than the PP model does. The primary reason for this is that more of the experimental data points were used in this study and our analytical solution provided more accuracy than the PP model. The use of the analytical solution is the reason for this improvement in accuracy. In this way, the analytical Jacobian matrix of V_{cell} with respect to parameters can be obtained directly from the algebraic expressions rather than from solving the differential equations. For the PP model, however, if the least square method is applied, a large number of coupled partial derivative equations will be added to the model in finding the numerical Jacobian matrix and the computation may get extremely slow and difficult; for this reason, the parameter estimation in Ref. 15 was performed only with the methods that are faster but with less accuracy, such as locating the characteristic points on the discharge curves. The C/33 discharge curves at different temperatures are plotted in Fig. 3e with the reaction entropy change $(\partial U_p/\partial T - \partial U_n/\partial T)$ curve. As shown in Fig. 3e, the $(\partial U_p/\partial T - \partial U_n/\partial T)$ value is positive at the initial stage of discharge, so the cell at high temperature has higher voltage. As discharge goes on, the $(\partial U_p/\partial T - \partial U_n/\partial T)$ value reduces to zero and then negative and the difference between the curves gets smaller. At the end of discharge, the deviation between the discharge capacities is determined by the difference in the initial states of charge.

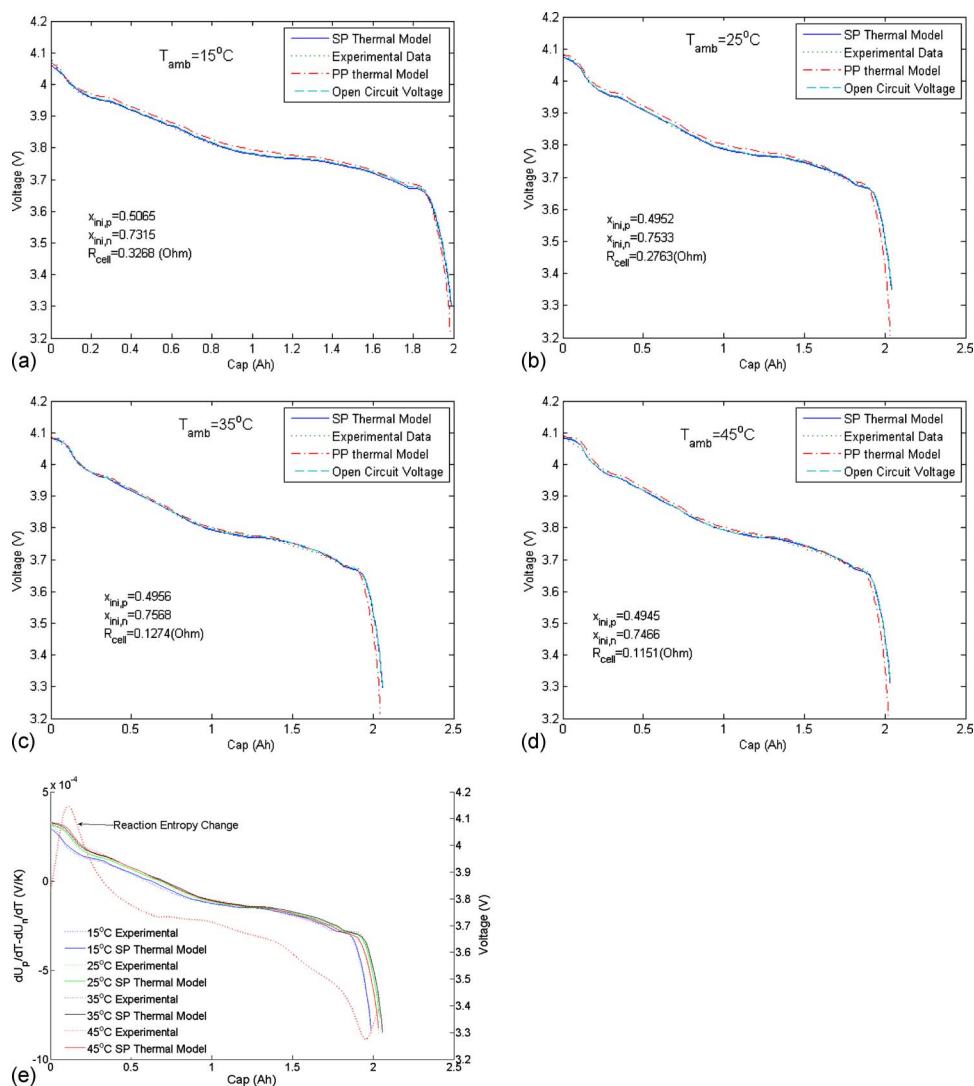


Figure 3. (Color online) Comparison between simulated and experimental discharge profiles at C/33. The experimental data were obtained from lithium-ion pouch cells discharged at corresponding rates to a cutoff potential of 3.0 V. (a) 15°C , (b) 25°C , (c) 35°C , (d) 45°C and (e) C/33 discharge profiles at for temperatures with reaction entropy change curve.

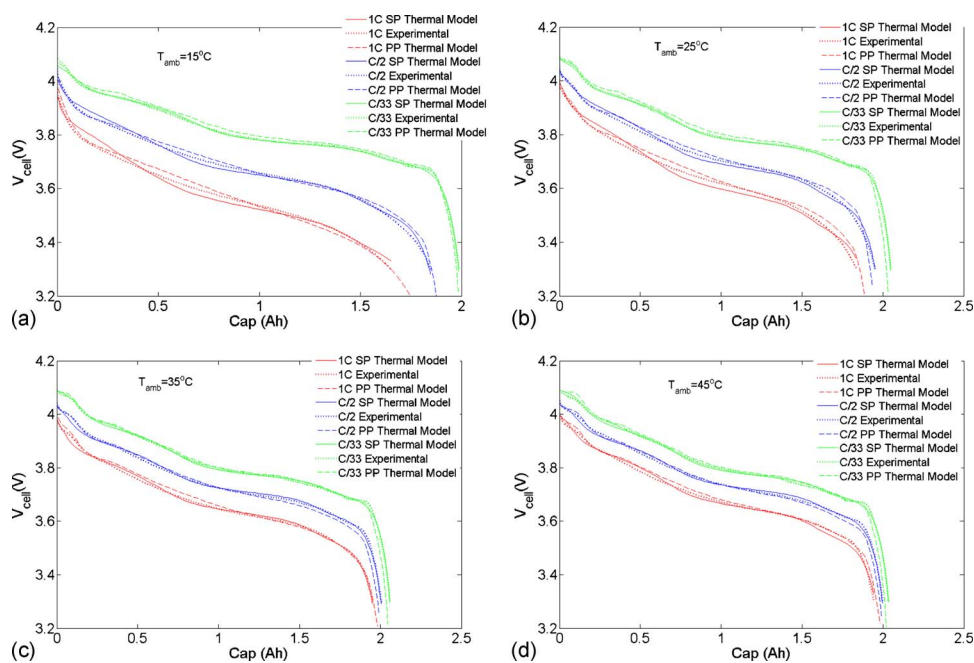


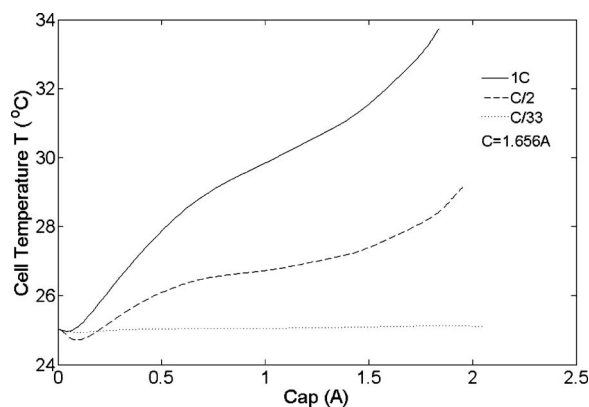
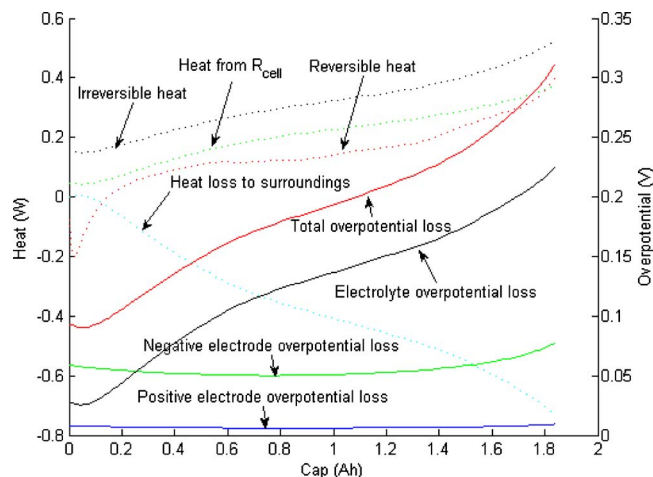
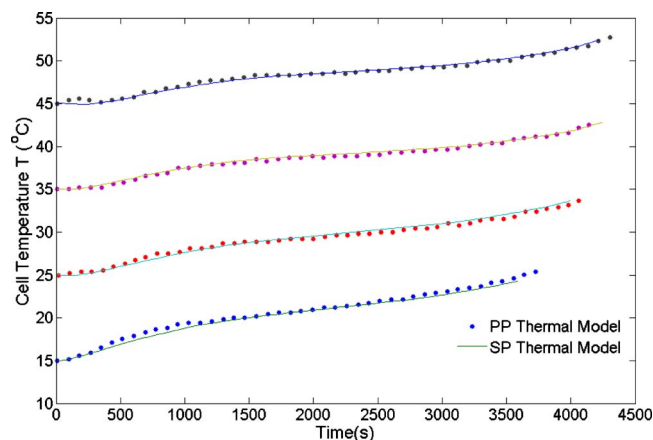
Figure 4. (Color online) Comparison between simulated and experimental discharge profiles at C/33, C/2, and 1C. The experimental data were obtained from lithium-ion pouch cells discharged at corresponding rates to a cutoff potential of 3.0 V. (a) 15°C , (b) 25°C , (c) 35°C , and (d) 45°C .

Table III. The parameter values estimated by fitting the C/2 and 1C discharge curves at different temperatures.

	C/2 ^a	1C ^a
15°C	$\theta_1 = 0.0188 \Omega$ $\theta_2 = 0.0473 \Omega/K$	$\theta_1 = 0.0222 \Omega$ $\theta_2 = 0.0150 \Omega/K$
25°C	$\theta_1 = 0.0199 \Omega$ $\theta_2 = 0.0392 \Omega/K$	$\theta_1 = 0.0159 \Omega$ $\theta_2 = 0.0137 \Omega/K$
35°C	$\theta_1 = 0.0428 \Omega$ $\theta_2 = 0.0085 \Omega/K$	$\theta_1 = 0.0363 \Omega$ $\theta_2 = 0.0056 \Omega/K$
45°C	$\theta_1 = 0.0398 \Omega$ $\theta_2 = 0.0049 \Omega/K$	$\theta_1 = 0.0298 \Omega$ $\theta_2 = 0.0061 \Omega/K$

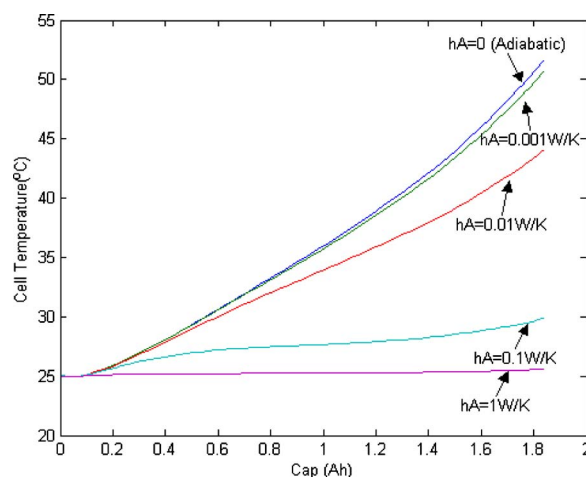
^a Where C = 1.656 Ah

Comparisons for discharge profiles at all the rates and temperatures are presented in Figs. 4a-4d. (The C/33 discharge curves shown in Fig. 3 are also presented in this figure with C/2 and 1C curves). The parameter values estimated from C/2 and 1C curves are listed in Table III. The fitting parameters θ_1 and θ_2 with ambient temperature and applied current are given in Appendix C. As shown in Fig. 4, the single-particle thermal model shows good agreement with both the experimental data and the PP model predictions for a

**Figure 5.** The temperature profiles for C/33, C/2, and 1C discharges starting from 25 °C.**Figure 6.** (Color online) Variation of heat generation and overpotential for cell discharged with 1C rate and starting temperature of 25 °C.**Figure 7.** (Color online) Variation of cell temperature with 1C rate discharge for different starting temperatures simulated by the single-particle model and the PP model.

range of current rates and different cell temperatures. Inspection of Fig. 4b reveals that there is approximately 100 mV overpotential at the 1C rate. This overpotential is primarily due to the cell resistance, R_{cell} , and the kinetic resistance at the anode due to the relatively small value of k_n (see Table II). The experimental results at 35 and 45°C are similar; however, we included the data at both temperatures to be complete in comparison to Ref. 15.

The cell temperature.— The simulated cell temperature profiles on discharge starting at 25°C for different rates are presented in Fig. 5. As shown in these plots, for C/33 rate, the cell temperature almost remains constant. At higher rates, i.e., C/2 and 1C discharges, three regions were observed; in the beginning, the cell temperature drops slightly and then increases sharply; as the discharge goes further, the cell temperature keeps rising; and at the final stage of discharge, the cell temperature starts to increase rapidly again. This phenomenon can be explained from the energy balance equation in Eq. 16. In this case, the initial $\partial U_p/\partial T$ for the positive electrode (where $x_{ini,p} \approx 0.5$) is near a positive peak (see point A in Fig. 10a in Appendix A), and the initial $\partial U_n/\partial T$ value for the negative electrode (where $x_{ini,n} \approx 0.78$) is about -0.1 mV/K (see point B in Fig. 10b in Appendix A), so the reversible heat $IT[\partial U_p/\partial T(x_{ini,n}) - \partial U_n/\partial T(x_{ini,n})]$ at the initial stage of discharge could be a negative number with a larger magnitude than the irreversible heat (see Fig.

**Figure 8.** (Color online) Variation of cell temperature in 1C discharge with different hA values and a starting temperatures of 25 °C.

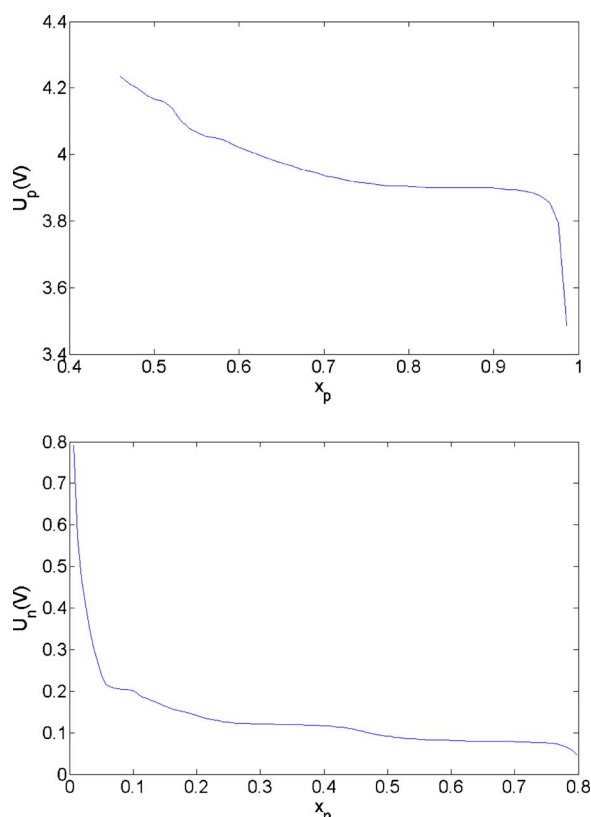


Figure 9. (Color online) The OCP profiles for (a) positive and (b) negative electrodes.

6) and hence causes the cell temperature to drop. Such a drop in the cell temperature was also observed experimentally in Ref. 20. As the discharge continues, the surface SoC for the positive electrode $x_{p,surf}$ gets larger and passes the peak shown in Fig. 10a and the $\partial U_p / \partial T$ turns to negative; accordingly, the reversible heat term becomes positive (see Fig. 6) and the cell temperature increases significantly with the joint effects of the both the irreversible heat and the positive reversible heat. While the cell temperature goes up, the increasing temperature difference between the cell and surrounding accelerates heat dissipation, which in turn prevents an accelerated rise in the temperature. At the final stage of discharge, the surface SoC for the negative electrode $x_{n,surf}$ drops to close to 0, and the irreversible heat gets large quickly due to a sharp increase in the magnitude of the overpotential, so the cell temperature goes up rapidly again. A useful quantity that can be defined is the ratio of reversible heat to irreversible heat

$$\frac{\text{Reversible Heat}}{\text{Irreversible Heat}} = \frac{IT \left[\frac{\partial U_p}{\partial T}(x_{p,surf}) - \frac{\partial U_n}{\partial T}(x_{n,surf}) \right]}{I(\eta_p - \eta_n + IR_{cell})} \quad [35]$$

When current increases, the magnitude of electrode overpotential (the denominator in Eq. 35) gets large, so the ratio in Eq. 35 decreases; this means that the contribution of the reversible heat becomes less significant than that of the irreversible heat for higher current. Using such a conclusion, we can explain why the temperature curve of the C/2 discharge has a larger drop than that of the 1C discharge at the initial stage. Figure 6 also shows that the total cell over voltage is mainly determined by the negative electrode overpotential and potential loss on R_{cell} , and these two parts are also the major source of irreversible heat.

The simulated cell temperature profiles during 1C discharge for different ambient temperatures are shown in Fig. 7. By comparing these results with those from the PP model, we obtain the value for

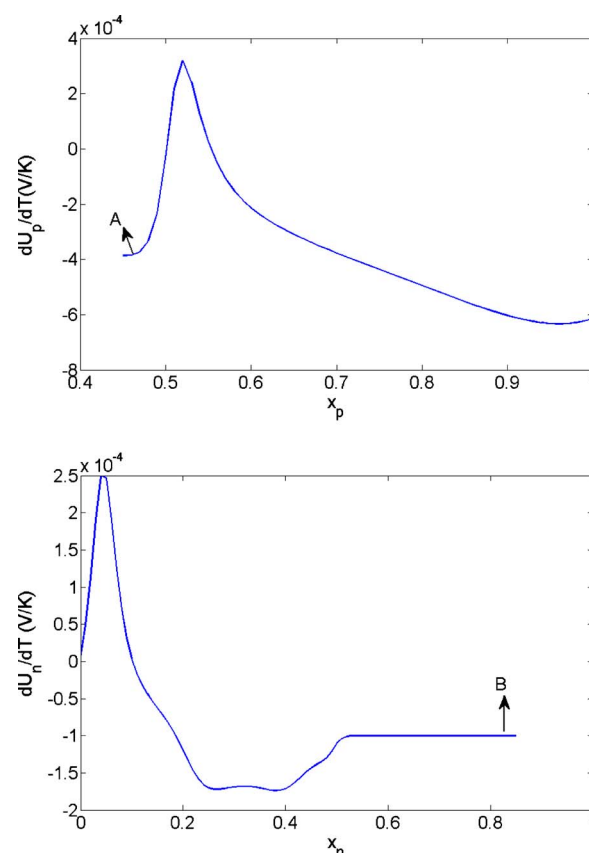


Figure 10. (Color online) The entropy change coefficient profiles for (a) positive and (b) negative electrodes.

heat transfer coefficient times the cell surface area $hA = 0.085 \text{ W/K}$. For the single-particle model, the temperature rise during the entire discharge $T|_{t=t_{final}} - T|_{t=0}$ with an initial temperature of 15°C is 9.3°C whereas that with an initial temperature of 45°C is only 7.4°C . The PP model results from Ref. 14 also show that the difference $T|_{t=t_{final}} - T|_{t=0}$ decreases as the initial temperature gets higher.

This single-particle thermal model was also used to simulate the discharge with adiabatic conditions. Figure 8 shows the temperature profiles for cell discharged with different hA values at 1C rate and an initial temperature of 25°C . As shown in Fig. 8, the cell temperature increases by 30°C at the adiabatic condition ($hA = 0$), but the cell temperature remains almost constant for large hA values (e.g., more than 1 W/K). So the heat transfer conditions have a very significant effect on the cell's thermal behavior.

Conclusion

The single-particle model was extended to include an energy balance. The model shows good agreement with the PP model as well as the experimental data for various rates and temperatures. The model offers good advantage in terms of computational efficiency over the PP model. Consequently, the model developed in this work can be readily used to simulate the cycling conditions for cells and battery packs.

University of South Carolina assisted in meeting the publication costs of this article.

Appendix A

The OCP profiles for Li_xCoO_2 and MCMB obtained from Ref. 14 are presented in Fig. 9. The expressions for the OCP as the functions of state of charge are obtained from fitting the experimental curves. For the positive electrode

$$U_p = 4.04596 + \exp(-42.30027x_p + 16.56714) - 0.04880 \arctan(50.01833x_p - 26.48897) - 0.05447 \arctan(18.99678x_p - 12.32362) - \exp(78.24095x_p - 78.68074) \quad [A-1]$$

where the surface state of charge of the positive electrode x_p equals to the stoichiometric value x in Li_xCoO_2 ; and for the negative electrode

$$U_n = 0.13966 + 0.68920 \exp(-49.20361x_n) + 0.41903 \exp(-254.40067x_n) - \exp(49.97886x_n - 43.37888) - 0.028221 \arctan(22.52300x_n - 3.65328) - 0.01308 \arctan(28.34801x_n - 13.43960) \quad [A-2]$$

where the surface state of charge of the negative electrode x_n equals to the stoichiometric value y in Li_yC_6 . In these two equations, U_p and U_n have the unit of volts.

The entropy coefficient profiles for Li_xCoO_2 and MCMB obtained from Ref. 8 are presented in Fig. 10. The expressions for the OCP as the functions of state of charge are obtained from fitting the experimental curves. For the positive electrode

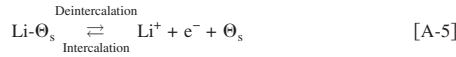
$$\frac{\partial U_p}{\partial T} = \frac{-0.19952 + 0.92837x_p - 1.36455x_p^2 + 0.61154x_p^3}{1 - 5.66148x_p + 11.47636x_p^2 - 9.82431x_p^3 + 3.04876x_p^4} \quad [A-3]$$

where the surface state of charge of the positive electrode x_p equals to the stoichiometric value x in Li_xCoO_2 ; and for the negative electrode

$$\frac{\partial U_n}{\partial T} = \frac{(0.00527 + 3.29927x_n - 91.79326x_n^2 + 1004.91101x_n^3 - 5812.27813x_n^4 + 19,329.75490x_n^5 - 37,147.89470x_n^6 + 38,379.18127x_n^7 - 16,515.05308x_n^8)}{(1 - 48.09287x_n + 1017.23480x_n^2 - 10,481.80419x_n^3 + 59,431.30001x_n^4 - 195,881.64880x_n^5 + 374,577.31520x_n^6 - 385,821.16070x_n^7 + 165,705.85970x_n^8)} \quad [A-4]$$

where the surface state of charge of negative electrode x_n equals to the stoichiometric value y in Li_yC_6 . In these two equations, $\partial U_p/\partial T$ and $\partial U_n/\partial T$ have the units of millivolts per Kelvin.

The electrochemical reaction for the intercalation/deintercalation at a solid/solution interface can be written as



where $\text{Li-}\Theta_s$ represents a filled intercalation site and Θ_s represents an intercalation site.

The concentration of filled $\text{Li-}\Theta_s$ sites at the particle surface is assumed to be equal to the lithium-ion concentration at the surface

$$c_{\text{Li-}\Theta_s} = c_{s,j}|_{r=R_j} = x_{j,\text{surf}}c_{s,j,\text{max}} \quad [A-6]$$

The concentration of the sites Θ_s at the particle surface can be expressed as

$$c_{\Theta_s} = c_{s,j,\text{max}} - c_{s,j}|_{r=R_j} = (1 - x_{j,\text{surf}})c_{s,j,\text{max}} \quad [A-7]$$

The concentration of Li^+ in the solution phase is equal to the average electrolyte concentration, c_e .

The current density for the forward reaction rate (i.e., in the anodic reaction) is

$$\tilde{i}_j = \tilde{k}_j(T)Fc_{s,j,\text{max}}x_{j,\text{surf}} \exp\left[\frac{\alpha_{a,j}F}{RT}(\phi_{1,j} - \phi_{2,j})\right] \quad [A-8]$$

where \tilde{i}_j is the current density for the forward reaction of electrode j , $\tilde{k}_j(T)$ is the temperature-dependent rate constant for the forward reaction of electrode j , and $\alpha_{a,j}$ is the anodic transfer coefficient for the forward reaction of electrode j . And the current density for the reverse reaction rate (i.e., in the cathodic reaction) is

$$\tilde{i}_j = \tilde{k}_j(T)Fc_{s,j,\text{max}}c_e(1 - x_{j,\text{surf}}) \exp\left[-\frac{\alpha_{c,j}F}{RT}(\phi_{1,j} - \phi_{2,j})\right] \quad [A-9]$$

where \tilde{i}_j is the current density for the reverse reaction of electrode j , $\tilde{k}_j(T)$ is the temperature-dependent rate constant for the reverse reaction of electrode j , and $\alpha_{c,j}$ is the cathodic transfer coefficient for the reverse reaction of electrode j . The exchange current density of the electrochemical reaction is defined as the reaction current density at OCP ($\phi_{1,j} - \phi_{2,j} = U_j$)

$$i_{0,j} = \tilde{k}_j(T)Fc_{s,j,\text{max}}x_{j,\text{surf}} \exp\left[\frac{\alpha_{a,j}F}{RT}U_j\right] = \tilde{k}_j(T)Fc_{s,j,\text{max}}c_e(1 - x_{j,\text{surf}}) \exp\left[-\frac{\alpha_{c,j}F}{RT}U_j\right] \quad [A-10]$$

The exponential terms in Eq. A-10 can be removed

$$i_{0,j} = (i_{0,j})^{\alpha_{a,j}}(i_{0,j})^{\alpha_{c,j}} = [\tilde{k}_j(T)Fc_{s,j,\text{max}}x_{j,\text{surf}}]^{\alpha_{a,j}}[\tilde{k}_j(T)Fc_{s,j,\text{max}}c_e(1 - x_{j,\text{surf}})]^{\alpha_{c,j}} = [\tilde{k}_j(T)]^{\alpha_{a,j}}[\tilde{k}_j(T)]^{\alpha_{c,j}}(Fc_{s,j,\text{max}})^{\alpha_{a,j}+\alpha_{c,j}}c_e^{\alpha_{c,j}}x_{j,\text{surf}}^{\alpha_{a,j}}(1 - x_{j,\text{surf}})^{\alpha_{c,j}} \quad [A-11]$$

Assuming $\alpha_{a,j} + \alpha_{c,j} = 1$ and let

$$k_j = [\tilde{k}_j(T)]^{\alpha_{a,j}}[\tilde{k}_j(T)]^{\alpha_{c,j}} \quad [A-12]$$

Eq. A-11 then becomes

$$i_{0,j} = k_j(T)Fc_{s,j,\text{max}}c_e^{\alpha_{c,j}}x_{j,\text{surf}}^{\alpha_{a,j}}(1 - x_{j,\text{surf}})^{\alpha_{c,j}} \quad [A-13]$$

Equation A-13 is the same as Eq. 22 of Thomas et al.²¹ So the forward and reverse reaction current densities can be expressed in terms of the exchange current density

$$\tilde{i}_j = i_{0,j} \exp\left[\frac{\alpha_{a,j}F}{RT}(\phi_{1,j} - \phi_{2,j} - U_j)\right] \quad [A-14]$$

$$\tilde{i}_j = i_{0,j} \exp\left[-\frac{\alpha_{c,j}F}{RT}(\phi E - \phi_{2,j} - U_j)\right] \quad [A-15]$$

The overpotential of electrode j is defined as

$$\eta_j = \phi_{1,j} - \phi_{2,j} - U_j \quad [A-16]$$

then Eq. A-14 and A-15 become

$$\tilde{i}_j = i_{0,j} \exp\left(\frac{\alpha_{a,j}F}{RT}\eta_j\right) \quad [A-17]$$

$$\tilde{i}_j = i_{0,j} \exp\left(-\frac{\alpha_{c,j}F}{RT}\eta_j\right) \quad [A-18]$$

And the total reaction current density for the surface electrochemical reaction is

$$i_j = \tilde{i}_j - \tilde{i}_j = i_{0,j} \left[\exp\left(\frac{\alpha_{a,j}F}{RT}\eta_j\right) - \exp\left(-\frac{\alpha_{c,j}F}{RT}\eta_j\right) \right] = k_j(T)Fc_{s,j,\text{max}}c_e^{\alpha_{c,j}}x_{j,\text{surf}}^{\alpha_{a,j}}(1 - x_{j,\text{surf}})^{\alpha_{c,j}} \left[\exp\left(\frac{\alpha_{a,j}F}{RT}\eta_j\right) - \exp\left(-\frac{\alpha_{c,j}F}{RT}\eta_j\right) \right] \quad [A-19]$$

Assuming that $\alpha_{a,j} = \alpha_{c,j} = 0.5$, Eq. A-13 becomes

$$i_{0,j} = k_j(T)Fc_{s,j,\text{max}}c_e^{0.5}x_{j,\text{surf}}^{0.5}(1 - x_{j,\text{surf}})^{0.5} \quad [A-20]$$

and Eq. A-19 becomes

$$i_j = k_j(T)Fc_{s,j,\text{max}}c_e^{0.5}x_{j,\text{surf}}^{0.5}(1 - x_{j,\text{surf}})^{0.5} \left[\exp\left(\frac{0.5F}{RT}\eta_j\right) - \exp\left(-\frac{0.5F}{RT}\eta_j\right) \right] \quad [A-21]$$

Equation A-20 is the same as Eq. A-9 of Doyle and Newman, and Eq. A-21 is the same as Eq. A-7 of Doyle and Newman.²²

The flux of lithium at the electrode surface

$$J_j = \frac{i_j}{F} = k_j(T)c_{s,j,\text{max}}c_e^{0.5}x_{j,\text{surf}}^{0.5}(1 - x_{j,\text{surf}})^{0.5} \left[\exp\left(\frac{0.5F}{RT}\eta_j\right) - \exp\left(-\frac{0.5F}{RT}\eta_j\right) \right] \quad [A-22]$$

Appendix B

The Eigenfunction Expansion Method

In the thermal model, the diffusion coefficient $D_{s,j}$ is assumed to be a function of time only, and the governing equation for solid phase diffusion (Eq. 1) can be rewritten as

$$\frac{\partial x_i}{\partial t} = \frac{D_{s,j}(t)}{R_j^2} \frac{1}{r_j^2} \frac{\partial}{\partial r_j} \left(r_j^2 \frac{\partial x_i}{\partial r_j} \right) \quad [B-1]$$

and the initial and boundary conditions become

$$t = 0, \quad x_j = x_{j,\text{ini}}$$

$$\bar{r}_j = 0, \quad \frac{\partial x_i}{\partial \bar{r}_j} = 0$$

$$\bar{r}_j = 1, \quad \frac{\partial x_i}{\partial \bar{r}_j} = -\frac{J_j R_j}{c_{s,j,\text{max}} D_{s,j}(t)} = \delta_j(t)$$

where J_j has been defined in Eq. 5.

We can use the following transformation to make the boundary conditions homogeneous

$$x_j(\bar{r}_j, t) = \frac{\delta_j(t)}{2} \bar{r}_j^2 + C(t) + w(\bar{r}_j, t) \quad [B-2]$$

where the variable w can be expanded in a Fourier series

$$w(\bar{r}_j, t) = \sum_{k=1}^{\infty} \alpha_k(t) z_k(\bar{r}_j) \quad [\text{B-3}]$$

and z_k satisfies

$$z_k(\bar{r}_j) = \frac{1}{\bar{r}_j^2} \frac{\partial}{\partial \bar{r}_j} \left(\bar{r}_j^2 \frac{\partial z_k(\bar{r}_j)}{\partial \bar{r}_j} \right) \quad [\text{B-4}]$$

$$\bar{r}_j = 0, \quad \frac{\partial z_k(\bar{r}_j)}{\partial \bar{r}_j} = 0 \quad \bar{r}_j = 1, \quad \frac{\partial z_k(\bar{r}_j)}{\partial \bar{r}_j} = 0$$

Solving for Eq. B-4, we obtain

$$z_k(\bar{r}_j) = \frac{\sin(\lambda_k \bar{r}_j)}{\bar{r}_j} \quad [\text{B-5}]$$

where the eigenvalues λ_k are roots of the following equation

$$\sin \lambda_k - \lambda_k \cos \lambda_k = 0 \quad [\text{B-6}]$$

So

$$x_j = \frac{\delta_j(t)}{2} \bar{r}_j^2 + C(t) + \sum_{k=1}^{\infty} \alpha_k(t) \frac{\sin(\lambda_k \bar{r}_j)}{\bar{r}_j} \quad [\text{B-7}]$$

$C(t)$ can be determined from the volume-average method. The volume-average of variable x_j is

$$x_{j,\text{ave}} = \int_0^1 3\bar{r}_j^2 x_j d\bar{r}_j \quad [\text{B-8}]$$

From the governing equation B-1, we can obtain

$$\frac{dx_{j,\text{ave}}}{dt} = \frac{3D_{s,j}(t)}{R_j^2} \left(\bar{r}_j^2 \frac{\partial x_j}{\partial \bar{r}_j} \Big|_{\bar{r}_j=1} - \bar{r}_j^2 \frac{\partial x_j}{\partial \bar{r}_j} \Big|_{\bar{r}_j=0} \right) = \frac{3\delta_j(t)}{R_j^2} D_{s,j}(t) \quad [\text{B-9}]$$

and from Eq. B-7, we can obtain

$$\frac{dx_{j,\text{ave}}}{dt} = \frac{3}{10} \frac{d\delta_j(t)}{dt} + \frac{dC(t)}{dt} \quad [\text{B-10}]$$

By comparing Eq. B-9 and B-10, we can obtain

$$C(t) = C(0) - \frac{3\delta_j(t)}{10} + \frac{3\delta_j(0)}{10} + 3 \int_0^t \frac{D_{s,j}(\tau)}{R_j^2} \delta_j(\tau) d\tau \quad [\text{B-11}]$$

At time $t = 0$,

$$x_{j,\text{ini}} = \frac{\delta_j(0)}{2} \bar{r}_j^2 + C(0) + \sum_{k=1}^{\infty} \alpha_k(0) \frac{\sin(\lambda_k \bar{r}_j)}{\bar{r}_j} \quad [\text{B-12}]$$

Multiply both sides of Eq. B-12 by $3\bar{r}_j^2$ and integrate from 0 to 1 and obtain

$$C(0) = x_{j,\text{ini}} - \frac{3\delta_j(0)}{10} \quad [\text{B-13}]$$

The value of $\alpha_k(0)$ can be determined from orthogonality of the series. Multiplying both sides of Eq. B-12 by $\bar{r}_j \sin(\lambda_k \bar{r}_j)$ and integrating from 0 to 1, we get

$$\alpha_k(0) = - \frac{2\delta_j(0)}{\lambda_k^2 \sin(\lambda_k)} \quad [\text{B-14}]$$

Substitute Eq. B-11 and B-13 into Eq. B-7

$$x_j = x_{j,\text{ini}} + \frac{\bar{r}_j^2}{2} \delta_j(t) - \frac{3}{10} \delta_j(t) + 3 \int_0^t \left[\frac{D_{s,j}(\tau)}{R_j^2} \delta_j(\tau) \right] d\tau + \sum_{k=1}^{\infty} \alpha_k(t) \frac{\sin(\lambda_k \bar{r}_j)}{\bar{r}_j} \quad [\text{B-15}]$$

Substitute Eq. B-15 into Eq. B-1, then multiply both sides by $r \sin(\lambda_k \bar{r})$ and integrate from 0 to 1 to get

$$\frac{d\alpha_k(t)}{dt} + \frac{\lambda_k^2 D_{s,j}(t)}{R_j^2} \alpha_k(t) + \frac{2}{\lambda_k^2 \sin(\lambda_k)} \frac{d\delta_j(t)}{dt} = 0 \quad [\text{B-16}]$$

Now take the following transformation

$$u_{j,k}(t) = \sin(\lambda_k) \alpha_k(t) + \frac{2\delta_j(t)}{\lambda_k^2} \quad [\text{B-17}]$$

and substitute Eq. B-17 into Eq. B-15, B-16, and B-14 to obtain

$$x_j = x_{j,\text{ini}} + \frac{\bar{r}_j^2}{2} \delta_j(t) - \frac{3}{10} \delta_j(t) + 3 \int_0^t \left[\frac{D_{s,j}(\tau)}{R_j^2} \delta_j(\tau) \right] d\tau + \sum_{k=1}^{\infty} \frac{\sin(\lambda_k \bar{r}_j)}{\bar{r}_j \sin(\lambda_k)} \left[u_{j,k}(t) - \frac{2\delta_j(t)}{\lambda_k^2} \right] \quad [\text{B-18}]$$

$$\frac{du_{j,k}(t)}{dt} = - \frac{\lambda_k^2 D_{s,j}(t)}{R_j^2} u_{j,k}(t) + 2 \frac{D_{s,j}(t)}{R_j^2} \delta_j(t) \quad [\text{B-19}]$$

$$u_{j,k}|_{t=0} = 0$$

$$k = 1, \dots, \infty$$

$$j = p, n \quad [\text{B-20}]$$

Appendix C

The parameter θ_1 and θ_2 values listed in Table III are fit as functions of the ambient temperature T_{amb} and the applied current I_{app} , and the fitting equations are as follows:

$$\theta_1 = (-5.636 \times 10^{-7} I_{\text{app}} - 7.283 \times 10^{-6})(T_{\text{amb}} - 273.15)^3 + (5.676 \times 10^{-5} I_{\text{app}} + 6.453 \times 10^{-4})(T_{\text{amb}} - 273.15)^2 + (-2.221 \times 10^{-3} I_{\text{app}} - 1.635 \times 10^{-2})(T_{\text{amb}} - 273.15) + (2.437 \times 10^{-2} I_{\text{app}} + 1.428 \times 10^{-1}) \quad [\text{C-1}]$$

$$\theta_2 = (-6.824 \times 10^{-6} I_{\text{app}} + 1.372 \times 10^{-5})(T_{\text{amb}} - 273.15)^3 + (6.054 \times 10^{-4} I_{\text{app}} - 1.216 \times 10^{-3})(T_{\text{amb}} - 273.15)^2 + (-1.497 \times 10^{-2} I_{\text{app}} + 3.025 \times 10^{-2})(T_{\text{amb}} - 273.15) + (7.179 \times 10^{-2} I_{\text{app}} - 1.456 \times 10^{-1}) \quad [\text{C-2}]$$

List of Symbols

A	total cell surface area exposed to surroundings, m ²
Cap	capacity of cell, Ah
c_e	concentration of electrolyte in solution phase, mol/m ³
C_p	specific heat capacity of cell, J/kg/K
$c_{s,j}$	concentration of lithium in the intercalation particles of electrode j, mol/m ³
$c_{s,\text{ini},j}$	initial concentration of lithium ions in the intercalation particles of electrode j, mol/m ³
$c_{s,j,\text{max}}$	maximum concentration of lithium ions in the intercalation particles of electrode j, mol/m ³
$D_{s,j}$	solid phase diffusion coefficient of lithium ions in the intercalation particles of electrode j, m ² /s
$D_{s,j,\text{ref}}$	solid phase diffusion coefficient of lithium ions in the intercalation particles of electrode j at reference temperature, m ² /s
$E_{a,d,j}$	activation energy for solid phase diffusion coefficient of electrode j, kJ/mol
$E_{a,r,j}$	activation energy for reaction rate constant of electrode j, kJ/mol
F	Faraday's constant, 96,487 C/mol
h	heat transfer coefficient between cell and surroundings, W/m ² /K
I	applied current, A
J_j	flux of lithium ions on the surface of intercalation particles, mol/m ² /s
k_j	rate constant for the electrochemical reaction of electrode j, m ^{2.5} /mol ^{0.5} /s
$k_{j,\text{ref}}$	rate constant for the electrochemical reaction of electrode j at reference temperature, m ^{2.5} /mol ^{0.5} /s
L_j	thickness of active material on electrode j
L_s	thickness of separator
m_i	ratio of applied current density to exchange current density of electrode i
Q	rate of heat transfer between cell and surroundings, W
r	radial coordinate in the spherical intercalation particle, m
\bar{r}_j	$\bar{r}_j = r/R_j$, dimensionless radial coordinate in the spherical intercalation particle j
R	ideal gas constant, 8.3143 J/mol/K
R_{cell}	solution phase resistance, Ω
R_j	radius of spherical intercalation for electrode j, m
S_j	total electroactive area of electrode j, m ²
t	time, s
t_{final}	time at the end of discharge, s
T	temperature of cell, K or °C
T_{amb}	ambient temperature, K or °C
T_{ref}	reference temperature, 25°C
U_j	OCV of electrode j, V
$u_{j,k}$	the kth eigenfunction of electrode j, dimensionless
v	volume of cell, m ³
V_{cell}	voltage of cell, V

V_j	total volume of electrode j, m ³
x_j	state of charge of electrode j
$x_{\text{ini},j}$	initial state of charge of electrode j
$x_{j,\text{surf}}$	state of charge on the surface of intercalation particles of electrode j
Greek	
$\alpha_{a,j}$	anodic transfer coefficient of electrode j
$\alpha_{c,j}$	cathodic transfer coefficient of electrode j
$\delta_j(t)$	$\delta_j(t) = -J_j R_j / D_{s,j}(t) c_{s,j,\text{max}}$, dimensionless flux of lithium ions at electrode j
ε_j	volume fraction of solid phase active material in electrode j
η_j	overpotential of electrode j, V
θ_1	parameter used in approximated solution resistance, Ω
θ_2	parameter used in approximated solution resistance, Ω/K
λ_k	the k th eigenvalue
ρ	density of cell, kg/m ³
τ	dummy variable of integration, s
$\phi_{1,j}$	solid phase potential of electrode j, V
$\phi_{2,j}$	solution phase potential of electrode j, V
Subscripts	
ini	initial state
j	positive (p) and negative (n) electrodes
k	k th term in the solution series
s	solid phase
surf	at the surface of an intercalation particle

References

1. C. R. Pals and J. Newman, *J. Electrochem. Soc.*, **142**, 3274 (1995).
2. C. R. Pals and J. Newman, *J. Electrochem. Soc.*, **142**, 3282 (1995).
3. S. Santhanagopalan, Q. Guo, P. Ramadass, and R. E. White, *J. Power Sources*, **156**, 620 (2006).
4. G. Botte, B. Johnson, and R. E. White, *J. Electrochem. Soc.*, **146**, 914 (1999).
5. D. Bernardi, E. Pawlikowski, and J. Newman, *J. Electrochem. Soc.*, **132**, 5 (1985).
6. L. Rao and J. Newman, *J. Electrochem. Soc.*, **144**, 2697 (1997).
7. K. Nakamura, H. Ohno, K. Okamura, Y. Michihiro, I. Nakabayashib, and T. Kanashiro, *Solid State Ionics*, **135**, 143 (2000).
8. O. Egorkina and A. Skundin, *J. Solid State Electrochem.*, **2**, 216 (1998).
9. T. Kulova, A. Skundin, E. Nizhnikovskii, and A. Fesenko, *Russ. J. Electrochem.*, **42**, 259 (2006).
10. H. Zheng, J. Qin, Y. Zhao, T. Abe, and Z. Ogumi, *Solid State Ionics*, **176**, 2219 (2005).
11. V. Srinivasan and C. Y. Wang, *J. Electrochem. Soc.*, **150**, A98 (2003).
12. K. E. Thomas and J. Newman, *J. Power Sources*, **119–121**, 844 (2003).
13. K. E. Thomas, C. Bogatu, and J. Newman, *J. Electrochem. Soc.*, **146**, A570 (2001).
14. H. Yang and J. Prakash, *J. Electrochem. Soc.*, **151**, A1222 (2001).
15. K. Kumaresan, G. Sikha, and R. E. White, *J. Electrochem. Soc.*, **155**, A164 (2008).
16. G. Ning and B. N. Popov, *J. Electrochem. Soc.*, **151**, A1584 (2004).
17. J. Newman and C. W. Tobias, *J. Electrochem. Soc.*, **109**, 1183 (1962).
18. T. F. Fuller, M. Doyle, and J. Newman, *J. Electrochem. Soc.*, **141**, 1 (1994).
19. V. R. Subramanian and R. E. White, *J. Power Sources*, **96**, 385 (2001).
20. S. Al Hallaj, R. Venkatachalapathy, J. Prakash, and J. R. Selman, *J. Electrochem. Soc.*, **147**, 2432 (2000).
21. K. E. Thomas, J. Newman, R. M. Darling, in *Advances in Lithium-Ion Batteries*, W. A. van Schalkwijk and B. Scrosati, Editors, pp. 345–392, Kluwer Academic/Plenum Publishers, New York, NY (2002).
22. M. Doyle and J. Newman, *J. Electrochem. Soc.*, **143**, 1890 (1996).